Photonic spin-multiplexing metasurface for switchable spiral phase contrast imaging

Pengcheng Huo[1,2], Cheng Zhang[3,4], Wenqi Zhu[5,6], Mingze Liu[1], Song Zhang[1], Si Zhang[1], Lu Chen[5,6], Henri J. Lezec[5], Amit Agrawal[5,6], Yanqing Lu[1,2] and Ting Xu[1,2*]

1. *National Laboratory of Solid-State Microstructures, Jiangsu Key Laboratory of Artificial Functional Materials, College of Engineering and Applied Sciences, Nanjing University, Nanjing 210093, China*
2. *Collaborative Innovation Center of Advanced Microstructures, Nanjing 210093, China*
3. *School of Optical and Electronic Information, Huazhong University of Science and Technology, Wuhan 430074, China.*
4. *Wuhan National Laboratory for Optoelectronics, Huazhong University of Science and Technology, Wuhan 430074, China.*
5. *Physical Measurement Laboratory, National Institute of Standards and Technology, Gaithersburg, Maryland 20899, United States*
6. *Maryland NanoCenter, University of Maryland, College Park, Maryland 20899, United States*

* Email: xuting@nju.edu.cn

Abstract

As the two most representative operation modes in an optical imaging system, bright-field imaging and phase contrast imaging can extract different morphological information of an object. Developing a miniature and low-cost system capable of switching between these two imaging modes is thus very attractive for a number of applications, such as biomedical imaging. Here, we propose and demonstrate that a Fourier transform setup incorporating an all-dielectric metasurface can perform a two-dimensional spatial differentiation operation and thus achieve isotropic edge detection. In addition, the metasurface can provide two spin-dependent, uncorrelated phase profiles across the entire visible spectrum. Therefore, based on the spin-state of incident light, the system can be used for either diffraction-limited bright-field imaging or isotropic edge-enhanced phase contrast imaging. Combined with the advantages of planar architecture and ultrathin thickness of the metasurface, we envision this approach may open new vistas in the very interdisciplinary field of imaging and microscopy.

Keywords: Metasurface, phase contrast imaging, edge detection, orbital angular momentum

Fast and reliable detection and recognition of an object is one of the fundamental capabilities required in applications such as imaging, microscopy, machine learning and artificial intelligence. Although convectional bright-field imaging method can provide overall morphologies of amplitude objects, increasing image contrast and precisely distinguishing the edges of phase objects, such as certain biological samples that typically lack substantial amounts of natural pigments [1], is especially important. To enhance the optical imaging process, spatial filtering to modulate the input light field by placing an appropriate optical element in the incident beam path and changing its phase, amplitude and spatial frequency at the sample plane has been proposed [2]. Based on this operation, many phase contrast methods have been demonstrated, such as Zernike phase contrast imaging [3] and differential interference contrast imaging [4]. Recently, structured light to perform spatial differentiation for analog optical computing has shown the potentials for the application in image processing of edge detection [5-11]. However, most of the demonstrations on spatial differentiation are one-dimensional, which typically leads to anisotropic edge detection of object and thus is not perfectly suited to imaging applications.

With further studies on radial Hilbert transform filtering [12], it has been suggested that the opposite halves of any radial line of the spiral phase element will introduce a phase difference of π between the positive and negative spatial frequencies of incident light field, which leads to a strong isotropic edge contrast enhancement of observed amplitude and phase objects [13-16]. Since it only extracts important information and records basic geometric features related to the edges of an object, the spiral phase contrast imaging greatly reduces the amount of data to be processed. Till date, the primary realization of spiral phase contrast imaging is accomplished using a liquid crystal-based spatial light modulator, which offers dynamic control over the optical amplitude and phase at the expense of large volume, limited resolution and high cost [17-19]. Therefore, how to develop a miniature, high-resolution, low-cost and controllable spiral phase contrast imaging system for both amplitude and phase objects is very attractive for many practical applications.

In recent years, metasurfaces – ultrathin optical elements consisting of an array of subwavelength nanostructures – have attracted a lot of attention and made significant progress towards both the temporal and spatial domain manipulation of optical wavefronts [20-26]. These efforts push the engineering optics into a new era: Engineering Optics 2.0 [27,28]. Arbitrary control over the amplitude, phase, and polarization of light has been verified in various embodiments of nanophotonic devices such as metalenses [29,30], meta-

holograms [31,32], spin-to-orbital angular momentum conversion [33-39], imaging-based biosensor [40], nonlinear optics [41,42] and multispectral chiral imaging [43]. Here, by designing and embedding a photonic spin-multiplexing dielectric metasurface in the focal plane of a Fourier transform setup, we demonstrate that the system is capable of dynamically switching between the bright-field imaging mode and spiral phase contrast imaging mode only by changing the spin-state of incident light. The spiral phase filtering operation of the metasurface further enables two-dimensional spatial differentiation to the incident light field. As a result, it can be used for isotropic edge-enhanced detection of undyed biological samples. Combined with the advantages of planar architecture and ultrathin thickness offered by dielectric metasurface, this generalized method will expand its impact and open new possibilities of creating compact and low-cost multifunctional microscopes for biomedical imaging and surface defect detection.

In a Fourier transform setup (Fig. 1a), the electric field distribution of an incident plane wave illuminating an object can be written as $E_{in}(x, y)$. A spatial filter designed to physically implement a complex masking function $M(\rho, \phi)$ is placed at the Fourier plane of the lens 1. After passing through the filter and undergoing phase shift and amplitude transformation, the light field is reshaped by the lens 2, yielding an output electric field distribution $E_{out}(x, y)$ at the image plane. The output and input fields can be associated according to the following relation:

$$E_{out}(x, y) = E_{in}(x, y) \otimes m(r, \varphi) \tag{1}$$

Here, $(x,\ y)$ is the spatial coordinates at the object (image) plane and $(r,\ \varphi)$ is the corresponding polar coordinates. The symbol $\otimes$ represents convolution and $m(r, \varphi) = F\{M(\rho, \phi)\}$ denotes the Fourier transform of the masking function, which acts as the point-spread function (PSF). (ρ, ϕ) represents the polar coordinates in the Fourier plane and is related to cartesian coordinates $(u,\ v)$ in the Fourier plane as $\rho = \sqrt{u^2 + v^2}$ and $\phi = \tan^{-1}(v/u)$. Therefore, in principle, desirable light fields at the image plane can be achieved by modulating the masking function $M(\rho, \phi)$ of the spatial filter at the Fourier plane.

For example, for an object containing three rectangular slots illuminated by a plane wave, as shown in Fig. 1b, a masking function including a constant phase and amplitude $M_1(\rho, \phi) = \exp(ic_0)$, where c_0 is a constant, will generate a bright-field image at the image plane (Fig. 1c), like a conventional 4f imaging system. In contrast to the bright-field image, if the masking function becomes a spiral phase plate $M_2(\rho, \phi) = \exp(i\phi)$, the corresponding PSF $m_2(r, \varphi)$ can be regarded as the formation of a vortex that has a donut-shaped intensity distribution and a spiral phase profile changing from 0 to 2π for one turn

(Supplementary Note 1 for details). In the convolution process of eq. (1), m_2 with vortex element will be weighted to superimpose on each point of the input light field E_{in}, and then integrated over the whole area to determine the amplitude of the corresponding point of the output light field E_{out}. Due to the phase difference of π along the opposite azimuth of the vortex element, integrating the uniform area of E_{in} will lead to destructive interference and a dark background. In contrast, arbitrarily unevenness including amplitude gradient and phase gradient in the region of integration will remove this destructive interference and result in bright regions. In Fig. 1d, the calculated result of the image plane shows an isotropic effect of spiral phase contrast imaging, which is not sensitive to the absolute phase and amplitude of the object, but to the phase and amplitude gradients. In additional, the calculated spatial spectral transfer function is shown in supplementary Fig. S1. Combined with the analytical result of supplementary eq. (S7), it shows that spiral phase filtering operation is equivalent to two-dimensional spatial differentiation of the incident light field.

In synergy with the polarization states of incident light, ultrathin planar metasurface provides an effective approach to impart photonic spin-multiplexing phases at the Fourier plane. As a result, bright-field imaging and spiral phase contrast imaging can be dynamically switched by the chirality of light using metasurface spatial filter with spin-dependent masking functions. Assume the incident light upon the metasurface are in two orthogonal spin states $|L\rangle = \frac{1}{\sqrt{2}}\begin{bmatrix}1\\ i\end{bmatrix}$ and $|R\rangle = \frac{1}{\sqrt{2}}\begin{bmatrix}1\\ -i\end{bmatrix}$, where $|L\rangle$ and $|R\rangle$ denote left- and right-circular polarization (LCP and RCP) in the linear polarization basis. Fig. 1e and Fig. 1f show schematic of the concept for spin-multiplexing function control. In order to independently implement two uncorrelated masking functions (M_1 and M_2) for the incident plane wave propagating along the *z*-direction respectively in LCP and RCP states, the metasurface should simultaneously perform the beam transformation:

$$\text{LCP: } |L\rangle \rightarrow M_1|R\rangle \tag{2}$$

$$\text{RCP: } |R\rangle \rightarrow M_2|L\rangle \tag{3}$$

For LCP incident light, the metasurface spatial filter imprints a masking function (M_1) on the output beam with a constant phase profile and a Gaussian intensity distribution and flips the handedness of the incident polarization to RCP (Fig. 1e). On the other hand, for RCP incident light, the metasurface imprints another masking function (M_2) with a spiral phase profile and a donut-shaped intensity distribution, and again flips the handedness of the polarization to LCP (Fig. 1f). Consequently, the metasurface spatial filter can be expressed by a Jones matrix *J* which acts independently on the two orthogonal input states of light and takes the form:

$$J = \frac{1}{2}\begin{bmatrix} (M_1 + M_2) & -i(M_1 - M_2) \\ -i(M_1 - M_2) & -(M_1 + M_2) \end{bmatrix} \quad (4)$$

The unitary of this matrix guarantees that it can be diagonalized by solving the characteristic equation. The eigenvalues and eigenvectors of this Jones matrix require that the elements of the metasurface spatial filter have a birefringent response with the phase shifts (φ_x, φ_y) along the two perpendicular symmetry axes and the orientation angle θ of fast axes as a function of the reference coordinate. We can find the analytical expression for required phase shifts and orientation angles as follows (Supplementary Note 2 for details),

$$\varphi_x = \frac{1}{2}(c_0 + \phi) \quad (5)$$

$$\varphi_y = \frac{1}{2}(c_0 + \phi) - \pi \quad (6)$$

$$\theta = \frac{1}{4}(c_0 - \phi) \quad (7)$$

Therefore, it is imperative to find a set of nanostructures with proper phase shifts and orientation angles covering the full phase range [0, 2π].

Fig. 1g shows the schematic diagram of the proposed metasurface filter, which contains titanium dioxide (TiO_2) nanopillars arranged periodically in a square lattice with a constant $L_x = L_y =$ 450 nm. We choose TiO_2 as the constituent material because of its large index of refraction and low loss at visible frequencies (Supplementary Fig. S3). Each of these nanopillars have equal height (H = 600 nm) and acts as individual nanoscale half-wave plates (HWP). The propagation phase shifts φ_x and φ_y along the two symmetry axes are dependent on the in-plane dimensions D_x and D_y, and the geometric phase is controlled by the in-plane rotation angle θ of the fast axis of the nanopillar. Based on a suitable combination of propagation phase and geometric phase of the metasurface, two sets of uncorrelated phase profiles can be imparted on the incident light in its respective LCP and RCP states.

A broad range of TiO_2 rectangular nanopillars with a fixed height but varying in-plane dimensions are simulated to find the appropriate structural parameters for designing high efficiency HWP. Each point in the plot of transmission coefficients and phase shifts corresponds to a nanopillar with specific (D_x, D_y) combination for a particular wavelength (Supplementary Fig. S4). The degree of discretization of HWP in the full range [0, 2π] can be determined by calculating the mean square error function (*MSE*), which is used to evaluate the effect of segment number (s) in spiral phase on imaging quality as:

$$MSE(s) = \frac{\sum_{a=1}^{A}\sum_{b=1}^{B}|I(a,b) - I_s(a,b)|^2}{A \times B} \quad (8)$$

where $I(a,b)$ and $I_s(a,b)$ represent the imaging results by adopting an ideal and the s-segment spiral

phase filter, respectively. A and B are the pixel sampling number of the generated image along the *x* and *y* directions, respectively. Considering the trade-off between imaging quality and design complexity, the optimization operation yields $s = 16$ (Supplementary Note 3 for details). The structural parameters of a set of 16 nanopillars are optimized so that all the HWPs' transmission coefficients and polarization conversion efficiencies are sufficiently high across the entire visible region (Supplementary Fig. S9), which would benefit the imaging efficiency from the metasurface spatial filter. In addition, as shown in supplementary Fig. S10, the normalized energy density is mainly confined inside the TiO_2 nanopillar. The coupling effect between neighboring nanopillars is very weak, and thus each nanopillar can be regarded as an isolated rectangular waveguide. This makes the phase design for each nanopillar element still be accurate when they are arranged in a square lattice to form the metasurface spatial filter. Fig. 1h and 1i exhibit the optical photograph of the fabricated TiO_2 metasurface spatial filter of 2 mm diameter and the scanning electron microscope (SEM) images of the TiO_2 nanopillar array, respectively. The detailed fabrication process is described in the Methods section.

To fully characterize the two independent masking functions imposed on the spin-dependent metasurface spatial filter, the far-field intensity distributions and phase profiles of the output states have been numerically simulated and experimentally measured upon illumination with a circularly polarized Gaussian beam. At a free-space wavelength of 530 nm, the Gaussian intensity distribution (Fig. 2a) and a constant phase profile (Fig. 2b) demonstrate that the input Gaussian beam with LCP can pass through the metasurface spatial filter without any change except for flipping the handedness of the incident polarization. Once switching the incident light from LCP to RCP, the far-field output state shows a donut-shaped intensity distribution (Fig. 2c) and a spiral phase profile (Fig. 2d), indicating that the transmitted beam carries $1\hbar$ orbital angular momentum (OAM) while reversing the handedness. As shown in Fig. 2e and 2g, the experimentally measured intensity distributions for LCP and RCP incident light at wavelength of 530 nm are consistent with the simulated ones. To clarify the phase profiles, non-paraxial interference measurements have been carried out and the relevant results are shown in Fig. 2f for LCP light and Fig. 2h for RCP light. The interference patterns of equidistant stripes and fork-like stripes respectively demonstrate that the metasurface spatial filter endowed with the masking function M_1 and M_2 can independently shape the input chiral light to the desired states. Furthermore, the ability of spin-multiplexing metasurface spatial filter to shape incident light also has been experimentally demonstrated at other wavelengths of visible region

(Supplementary Fig. S11). The measured shaping efficiency of the metasurface spatial filter in the visible range can reach up to 50 % (Supplementary Fig. S12). This is mainly due to the low-loss material selection of TiO_2 and geometrical parameter optimization of HWPs, that are both helpful in improving the spatial filtering efficiency of the system.

The experimental setup for switchable spin-dependent bright-field and spiral phase contrast imaging is sketched in Fig. 3a. The sample is placed at the object plane and illuminated by a supercontinuum laser attached to an acousto-optic tunable filter (AOTF) system. A linear polarizer (LP) and a quarter-wave plate (QWP) are used to fully change the incident laser beam from linear polarization to circular polarization. A 20× microscope objective is used for image magnification. The rear focal plane of the objective is extended by using a relay system consisting of two lenses, and the metasurface spatial filter is placed at the Fourier plane. Between imaging lens and charge coupled device (CCD), a cross circularly polarizer (CP) is used to eliminate the background light that has the same handedness as the input beam.

To demonstrate the functionalities of the imaging system, a 1951 United State Air Force (USAF) resolution test chart is used as an imaging target and illuminated by the wavelength filtered supercontinuum laser. For the LCP incident beam at wavelengths of 480 nm, 530 nm, 580 nm, 630 nm, Fig. 3b-3e respectively display the bright-field images of fourth parts of the resolution test chart, which are recorded with a 20× magnification objective in transmission mode. These results correspond to the implementation of the constant phase masking function M_1 on the metasurface spatial filter. As the input polarization is switched from LCP to RCP, Fig. 3f-3i show the edge-enhanced images of the same target, achieved by implementing the spiral phase masking function M_2 on the metasurface spatial filter. Obviously, the contrast of all pattern edges is enhanced, irrespective of their orientations, which indicates the spiral phase contrast imaging is isotropic. In addition, the total light intensities between the bright-field image and phase contrast image are almost identical, revealing that the light energy is redistributed without loss in the phase contrast imaging operation. For the two typical imaging modes, the smallest line pair (lp) that can be resolved in the resolution test chart is elements 6 of group 7 (228 lp/mm) and elements 3 of group 7 (161 lp/mm), which corresponds a system resolution of 2.19 μm and 3.11 μm along all directions (Supplementary Fig. S13). In principle, the imaging resolution of the system can be improved by changing the objective lens and increasing the size of the metasurface spatial filter.

One major advantage of phase contrast imaging is that it can readily detect samples with small

refractive index difference from the background environment such as biological cells. Therefore, we further carry out the demonstration of switchable imaging of unstained onion epidermal cells with a 20× objective lens. Fig. 4a-4d show the bright-field images of onion epidermal cells captured with illumination of LCP light at wavelengths of 480 nm, 530 nm, 580 nm, 630 nm, respectively. Although one can see some organelles inside the cells, small amplitude and phase differences between cell walls and cytoplasm make the single cell boundary indistinguishable. However, the image contrast is completely changed in spiral phase contrast imaging upon illumination with RCP incident light (Fig. 4e-h). As expected, the edge-enhanced images reveal more details of cytoderm and make the single cell contour easy to identify, which would greatly benefit the cell morphological observation. Additionally, besides the wavelength filtered laser, even a broadband white light can be used as illumination source to achieve switchable bright-field and phase contrast imaging (Supplementary Fig. S14). This works not only because the implemented imaging system here is coaxial and contains achromatic lenses, but also due to the broadband response of the metasurface spatial filter across the entire visible frequency range.

In conclusion, we propose and demonstrate a spin-multiplexed metasurface-based optical imaging system capable of switching between bright-field and spiral phase contrast imaging modes. The metasurface spatial filter is formed by an array of subwavelength TiO_2 nanopillars and can provide two uncorrelated phase profiles corresponding to the spin states of the incident light. In the experiment, by imposing the metasurface spatial filter with a constant phase profile for LCP light and a spiral phase profile for RCP light, dynamically switchable ordinary diffraction imaging and isotropic edge-enhanced imaging are respectively demonstrated. Besides the photonic spin-controlled properties, the planar single layer and ultrathin architecture of the metasurface spatial filter realized here enables a scalable and integration friendly platform for structured light illumination, and its potential application in biomedical microscopy imaging, crystal dislocation detecting, and optical analog computing.

Methods

Numerical simulation

The numerical simulations shown in Fig.2 are performed using the finite-difference time-domain (FDTD) technique. The mesh grid on TiO_2 nanopillars in simulation is $g_x = g_y = g_z = 2$ nm. All the nanopillars have a fixed height of 600 nm. The phase shifts (φ_x, φ_y) are obtained by parameter sweeping of TiO_2 nanopillars'

in-plane dimension D_x and D_y varying from 100 nm to 400 nm with a step of 5 nm. The refractive index of TiO_2 is measured using spectroscopic ellipsometry (Supplementary Fig. S3).

Sample fabrications

Quartz substrates were first coated with hexamethyldisilazane and positive-tone electron beam resist. The resist thickness is 600 nm, which determines the height of the final TiO_2 nanopillars. Subsequently, samples were coated with 10 nm of aluminum via thermal evaporation to avoid charging effects during the electron-beam lithography step. The electron-beam lithography was done using an accelerating voltage of 125 kV and developed in hexyl acetate for 120 s. Next, the patterned samples were coated with TiO_2 using atomic layer deposition (ALD). The ALD was done at the temperature of 90 ℃ to ensure that the patterned resist does not deform. After this step, inductively-coupled-plasma reactive ion etching (ICP-RIE) was carried out with a mixture of Cl_2 and BCl_3 gas to etch the over-coated TiO_2 until the resist layer is reached. Finally, the samples were exposed to UV irradiation, followed by soaking in n-methyl-2-pyrrolidone. This step removes the resist and results in TiO_2 pillar arrays with pre-designed patterns.

Supporting Information

Derivation of spiral phase masking function, spatial spectral transfer function, derivation of the Jones matrix, calculation and simulation of phase modulation in dielectric nanopillars, spectroscopic ellipsometry measured refractive index of TiO_2, effect of the segment number of spiral phase on imaging, polarization conversion efficiency of the metasurface spatial filter, investigation of the system resolution, white light illuminated bright-field and phase contrast imaging of undyed onion epidermal cells.

Acknowledgements

The work is supported by the Key Research and Development Program from Ministry of Science and Technology of China (2016YFA0202100 and 2017YFA0303700) and National Natural Science Foundation of China (11774163). W. Z., L. C., A. A. acknowledge support under the Cooperative Research Agreement between the University of Maryland and the National Institute of Standards and Technology, Center for Nanoscale Science and Technology, Award#70-NANB14H209, through the University of Maryland.

Author Contributions

P. H., C. Z. and W. Z. contributed equally. All authors contributed to the interpretation of results and participated in manuscript preparation. T. X. directed the project.

Notes

The authors declare no competing financial interests.

References

[1] S. Bradbury and P. Evennett, *Contrast Techniques in Light Microscopy*, (BIOS Scientific, Oxford, 1996).

[2] J. W. Goodman, *Introduction to Fourier Optics*, *3rd Edition* (Roberts & Company Publishers, Englewood, CO, 2005).

[3] F. Zernike, and F. J. M. Stratton, Diffraction theory of the knife-edge test and its improved form, the phase-contrast method, *Mon. Not. R. Astron. Soc*. **94**, 377-384 (1934).

[4] G. Normanski, Interferometry with Schlieren microscopy, *J. Phys. Radium* **16**, 9-11 (1955).

[5] A. Silva, F. Monticone, G. Castaldi, V. Galdi, A. Alu, and N. Engheta, Performing mathematical operations with metamaterials, *Science* **343**,160-163 (2014).

[6] A. Pors, M. G. Nielsen, and S. I. Bozhevolnyi, Analog computing using reflective plasmonic metasurfaces, *Nano Lett.* **15**, 791–797 (2015).

[7] T. Zhu, Y. Zhou, Y. Lou, H. Ye, M. Qiu, Z. Ruan, and S. Fan, Plasmonic computing of spatial differentiation, *Nature communication* **8**, 15391 (2017).

[8] J. Zhou, H. Qian, C. Chen, J. Zhao, G. Li, Q. Wu, H. Luo, S. Wen, and Z. Liu, Optical edge detection based on high-efficiency dielectric metasurface, *Proc. Natl. Acad. Sci. USA* **116**, 11137-11140 (2019).

[9] T. Zhu, Y. Lou, Y. Zhou, J. Zhang, J. Huang, Y. Li, H. Luo, S. Wen, S. Zhu, Q. Gong, M. Qiu, and Z. Ruan, Generalized spatial differentiation from the spin hall effect of light and its application in image processing of edge detection, *Phys. Rev. Appl.* **11**, 034043 (2019).

[10] A. Cordaro, H. Kwon, D. Sounas, A. F. Koenderink, A. Alu, and A. Polman, High-index dielectric metasurfaces performing mathematical operations, *Nano Lett.* **19**, 8418-8423 (2019).

[11] Y. Zhou, H. Y. Zheng, I. I. Kravchenko, and J. Valentine, Flat optics for image differentiation, *Nature Photonics*, 1-9 (2020), https://doi.org/10.1038/s41566-020-0591-3

[12] J. A. Davis, D. E. McNamara, D. M. Cottrell, and J. Campos, Image processing with the radial Hilbert transform: theory and experiments, *Opt. Lett*. **25**, 99-101 (2000).

[13] G. A. Swartzlander, Jr., Peering into darkness with a vortex spatial filter, *Opt. Lett*. **26**, 497-499 (2001).

[14] K. Crabtree, J. A. Davis, and I. Moreno, Optical processing with vortex-producing lenses, *Appl. Opt*. **43**, 1360-1367 (2004).

[15] S. Furhapter, A. Jesacher, S. Bernet, and M. Ritsch-Marte, Spiral phase contrast imaging in microscopy, *Opt. Express* **13**, 689-694 (2005).

[16] A. Jesacher, S. Furhapter, S. Bernet, and M. Ritsch-Marte, Spiral interferogram analysis, *J. Opt. Soc. Am. A* **23**, 1400-1409 (2006).

[17] A. Jesacher, S. Furhapter, S. Bernet, and M. Ritsch-Marte, Shadow effects in spiral phase contrast microscopy, *Phys. Rev. Lett*. **94**, 233902 (2005).

[18] G. Situ, G. Pedrini, and W. Osten, Spiral phase filtering and orientation-selective edge detection/enhancement, *J. Opt. Soc. Am. A* **26**, 1788-1797 (2009).

[19] C. Maurer, A. Jesacher, S. Bernet, and M. Ritsch-Marte, What spatial light modulators can do for optical microscopy, *Laser Photonics Rev.* **5**, 81-101 (2011).

[20] D. Lin, P. Fan, E. Hasman, and M. L. Brongersma, Dielectric gradient metasurface optical elements, *Science* **345**, 298-302 (2014).

[21] A. Arbabi, Y. Horie, M. Bagheri, and A. Faraon, Dielectric metasurfaces for complete control of phase and polarization with subwavelength spatial resolution and high transmission, *Nat. Nanotech.* **10**, 937-943 (2015).

[22] S. Kruk, and Y. Kivshar, Functional meta-optics and nanophotonics governed by Mie resonances, *ACS Photonics* **4**, 2638-2649 (2017).

[23] P. Huo, S. Zhang, Y. Liang, Y. Lu and T. Xu, Hyperbolic metamaterials and metasurfaces: Fundamentals and applications, *Adv. Optical Mater.* **7**, 1801616 (2019).

[24] S. Divitt, W. Zhu, C. Zhang, H. J. Lezec, and A. Agrawal, Ultrafast optical pulse shaping using dielectric metasurfaces, *Science* **364**, 890-894 (2019).

[25] A. M. Shaltout, K. G. Lagoudakis, J. Groep, S. J. Kim, J. Vuckovic, V. M. Shalaev, and M. L. Brongersma, Spatiotemporal light control with frequency-gradient metasurfaces, *Science* **365**, 374-377 (2019).

[26] H. Kwon, E. Arbabi, S. M. Kamali, M. Fraaji-Dana, and A. Faraon, Single-shot quantitative phase gradient microscopy using a system of multifunctional metasurfaces, *Nat. Photonics* **14**, 109-114 (2020).

[27] X. G. Luo, Engineering optics 2.0: a revolution in optical materials, devices, and systems, *ACS Photonics* **5**, 4724-4738 (2018).

[28] X. G. Luo, Engineering Optics 2.0: A Revolution in Optical Theories, Materials, Devices and Systems, Springer Singapore, Singapore, (2019).

[29] M. Khorasaninejad, W. T. Chen, R. C. Devlin, J. Oh, A. Y. Zhu, and F. Capasso, Metalenses at visible wavelengths: Diffraction-limited focusing and subwavelength resolution imaging, *Science* **352**, 1190-1194 (2016).

[30] S. Wang, P. C. Wu, V. Su, Y. Lai, M. Chen, H. Y. Kuo, B. H. Chen, Y. H. Chen, T. Huang, J. Wang, R. Lin, C. Kuan, T. Li, Z. Wang, S. Zhu, and D. P. Tsai, A broadband achromatic metalens in the visible, *Nat. Nanotech.* **13**, 227-232 (2018).

[31] G. X. Zheng, H. Muhlenbernd, M. Kenney, G. X. Li, T. Zentgraf, and S. Zhang, Metasurface holograms reaching 80% efficiency, *Nat. Nanotech*, **10**, 308-312 (2015).

[32] B. Wang, F. Dong, Q. T. Li, D. Yang, C. Sun, J. Chen, Z. Song, L. Xu, W. Chu, Y. F. Xiao, Q. Cong, and Y. Li, Visible-frequency dielectric metasurfaces for multiwavelength achromatic and highly dispersive holograms, *Nano Lett.* **16**, 5235-5240 (2016).

[33] Y. Guo, M. Pu, Z. Zhao, Y. Wang, J. Jin, P. Gao, X. Li, X. Ma, and X. Luo, Merging geometric phase and plasmon retardation phase in continuously shaped metasurfaces for arbitrary orbital angular momentum generation, *ACS Photonics* **3**, 2022-2029 (2016).

[34] F. Zhang, M. Pu, J. Luo, H. Yu, and X. Luo, Symmetry breaking of photonic spin-orbit interactions in metasurfaces, *Opto-Electronic Engineering* **44**, 319-325 (2017).

[35] F. Zhang, M. Pu, X. Li, P. Gao, X. Ma, J. Luo, H. Yu, and X. Luo, All-dielectric metasurfaces for simultaneous giant circular asymmetric transmission and wavefront shaping based on asymmetric photonic spin-orbital interactions, *Adv. Funct. Mater.* **27**, 1704295 (2017).

[36] X. H. Ling, X. X. Zhou, K. Huang, Y. C. Liu, C. W. Qiu, H. L. Luo and S. C. Wen, Recent advances in the spin Hall effect of light, *Rep. Prog. Phys*. **80**, 066401 (2017).

[37] M. B. Pu, X. Li, X. L. Ma, Y. Q. Wang, Z. Y. Zhao, C. T. Wang, C. G. Hu, P. Gao, C. Huang, H. R. Ren, X. P. Li, F. Qin, J. Yang, M. Gu, M. H. Hong, and X. G. Luo, Catenary optics for achromatic generation

of perfect optical angular momentum, *Science Advances*, **1**, e1500396 (2015).

[38] P. Huo, S. Zhang, Q. Fan, Y. Lu, and T. Xu, Photonics spin-controlled generation and transformation of 3D optical polarization topologies enabled by all-dielectric metasurfaces, *Nanoscale* **11**, 10646-10654 (2019).

[39] Y. J. Bao, J. C. Ni, and C. W. Qiu, A minimalist single-layer metasurface for arbitrary and full control of vector vortex beams, *Adv. Mater*. **32**, 1905659 (2019).

[40] A. Tittl, A. Leitis, M. Liu, F. Yesilkoy, D. Y. Choi, D. N. Neshev, Y. S. Kivshar, and H. Altug, Imaging-based molecular barcoding with pixelated dielectric metasurfaces, *Science* **360**, 1105-1109 (2018).

[41] K. Koshelev, Y. T. Tang, K. F. Li, D. Y. Choi, G. X. Li, and Y. Kivshar, Nonlinear metasurfaces governed by bound states in the continuum, *ACS Photonics* **6**, 1639-1644 (2019).

[42] G. Hu, X. Hong, K. Wang, J. Wu, H. X. Xu, W. Zhao, W. Liu, S. Zhang, F. Garcia-Vidal, B. Wang, P. Lu, and C. W. Qiu, Coherent steering of nonlinear chiral valley photonics with a synthetic Au-WS_2 metasurface, *Nat. Photonics* **13**, 467-472 (2019).

[43] M. Khorasaninejad, W. T. Chen, A. Y. Zhu, J. Oh, R. C. Devlin, D. Rousso, and F. Capasso, Multispectral chiral imaging with a metalens, *Nano Lett.* **16**, 4595-4600 (2016).

Figure and caption

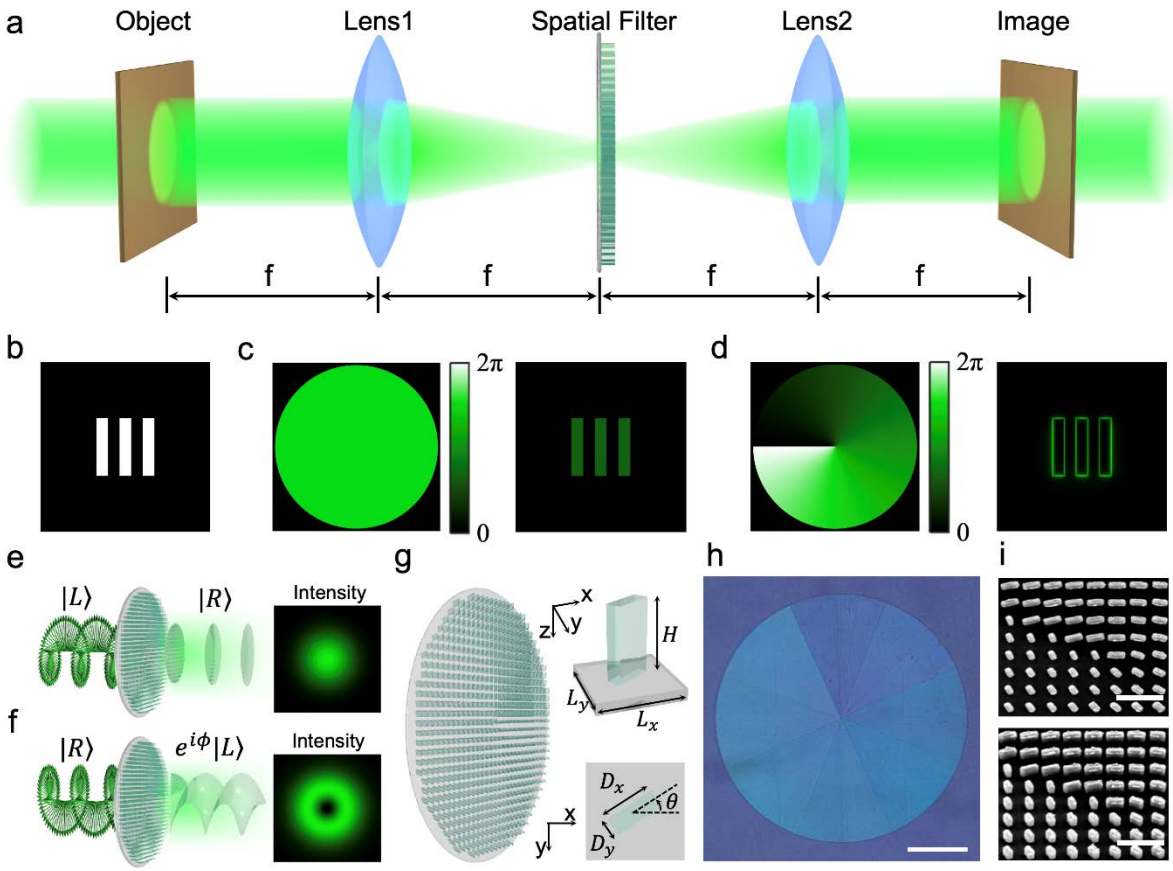

Figure 1. (a) Schematic of the Fourier transform setup for spatial filtering. An object (b) illuminated with a plane wave will diffract the light to outer regions in the Fourier plane, where the metasurface is placed. With a constant phase (c) or an ideal spiral phase (d) implemented in the metasurface, the calculated results of the image plane show a traditional bright image and an edge enhanced image. (e) and (f) Schematic of the concept for spin-dependent function control. (e) For light incident on the device with LCP, the metasurface imprints a masking function (M_1) on the output beam resulting in a constant phase profile and a Gaussian intensity distribution and flips the handedness of the incident polarization. (f) For light incident on the same device with RCP, the metasurface imprints another masking function (M_2), resulting in a spiral phase profile and a donut-shaped intensity distribution, and again flips the handedness of the polarization. (g) Schematic of the designed all-dielectric metasurface spatial filter to implement the function in (e) and (f). Inset: perspective and top view of the metasurface unit-cell formed by amorphous TiO_2 nanopillar sitting on a silica substrate. (h) Optical photograph of the fabricated metasurface device. Scale bar: 500 μm. (i) Top view and oblique view of the SEM images of TiO_2 nanopillar array. Scale bar: 1 μm.

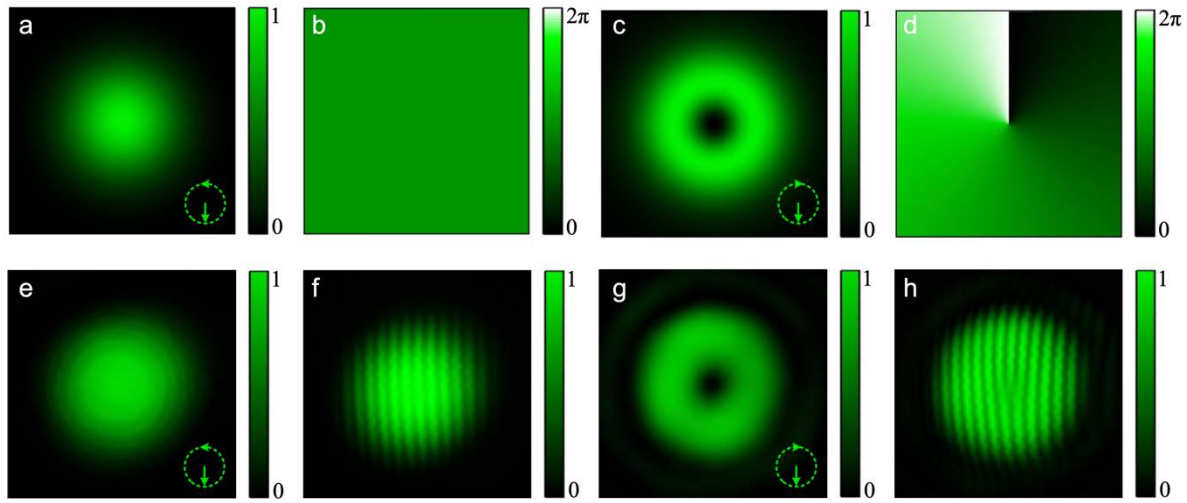

Figure 2. Simulated and experimental demonstration of the two independent masking functions imposed on the spin-dependent metasurface spatial filter. Upper: simulated output states of the metasurface spatial filter at the wavelength of 530 nm. An intensity distribution (a) and a phase profile (b) shows a Gaussian beam for LCP incident light, the donut intensity distribution (c) and the spiral phase profile (d) shows a $1\hbar$ OAM beam for RCP incident light. Below shows measured intensity distributions (e), (g) and non-paraxial interference patterns with a plane wavefront (f), (h) of output states corresponding to LCP and RCP incident light at the wavelength of 530 nm, respectively. Insets show the handedness of incident light.

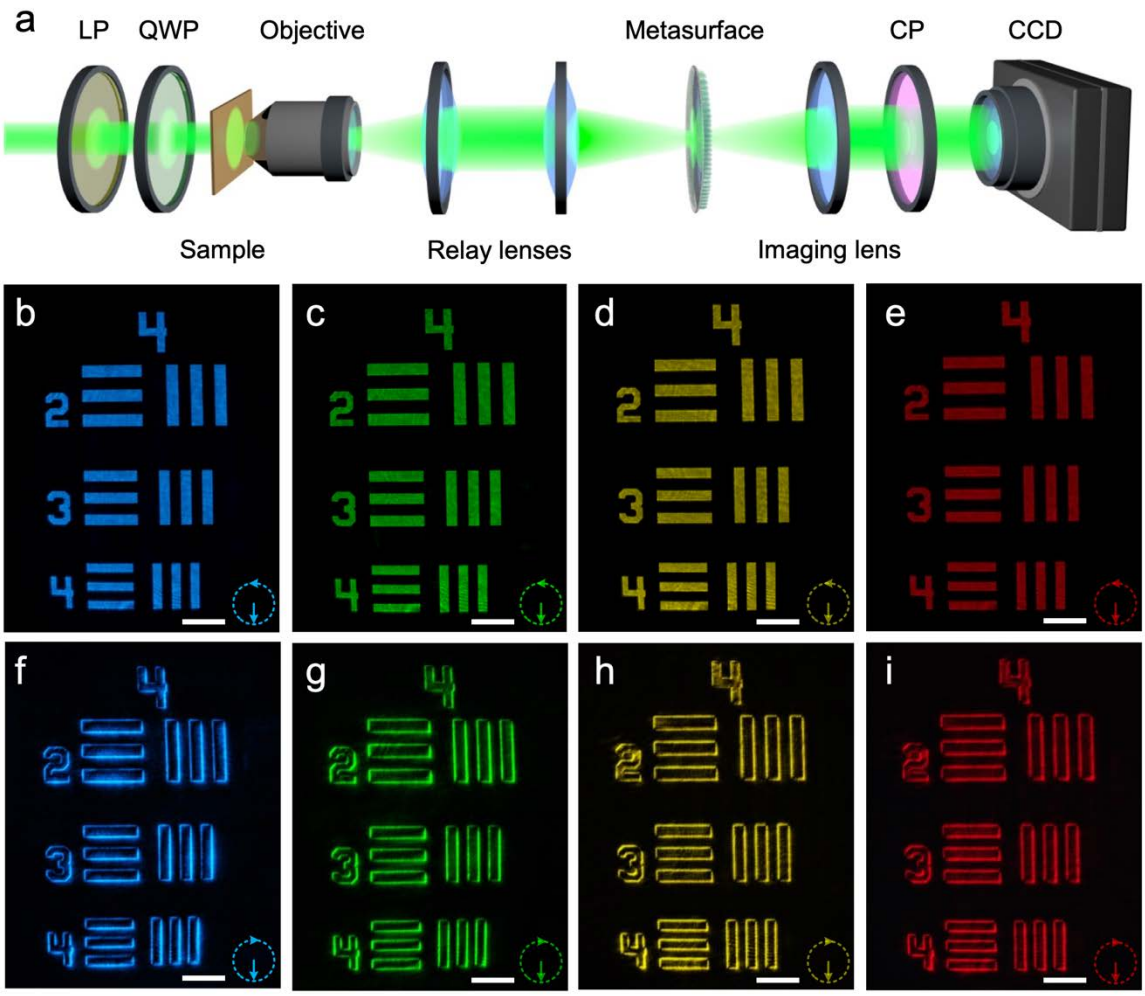

Figure 3. (a) Sketch of the experimental setup for spin-dependent spiral phase contrast imaging. LP and QWP can make the incident light with circular polarization. CP can be used to eliminate background light in the optical path. (b)-(e) The bright-field image of the resolution test chart under the LCP incident light at the wavelength of 480 nm, 530 nm, 580 nm, 630 nm, respectively. (f)-(i) Spiral phase contrast images of the resolution test chart under the RCP incident light at the same wavelengths. Insets show the handedness of incident light. Scale bars: 100 μm.

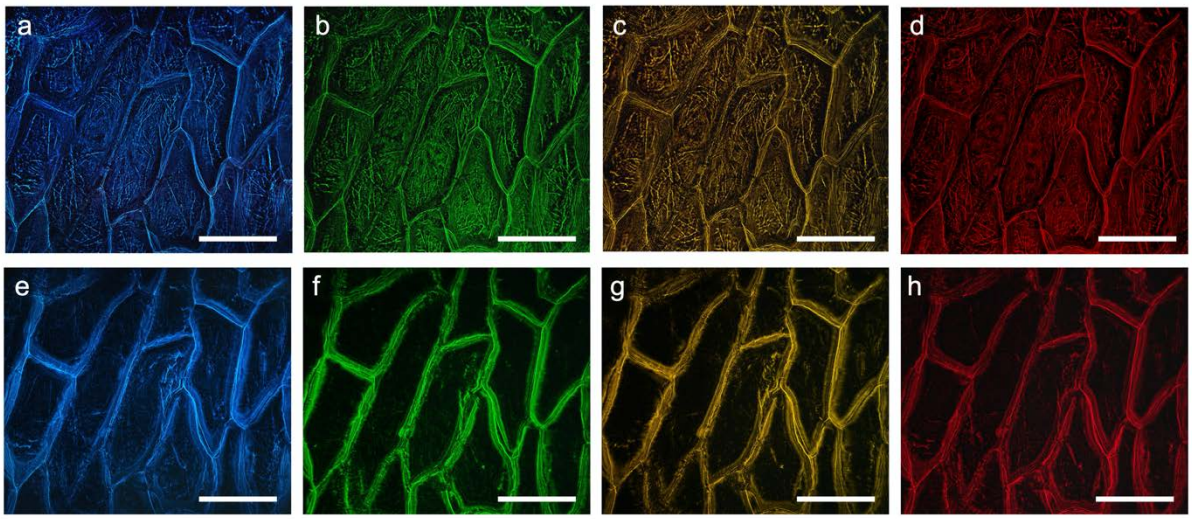

Figure 4. Images of the undyed onion epidermal cells with a 20 × objective lens. (a)-(d) Traditional bright-field images captured with LCP incident light at the wavelength of 480 nm, 530 nm, 580 nm, 630 nm, respectively. (e)-(h) Spiral phase contrast images captured with RCP incident light at the corresponding wavelengths. Scale bar: 100 μm.

Supporting Information

Photonic spin-multiplexing metasurface for switchable spiral phase contrast imaging

Pengcheng Huo[1], Cheng Zhang[2,3], Wenqi Zhu[4,5], Mingze Liu[1], Song Zhang[1], Si Zhang[1], Lu Chen[4,5], Henri J. Lezec[4], Amit Agrawal[4,5], Yanqing Lu[1] and Ting Xu[1]

1. *National Laboratory of Solid-State Microstructures, Jiangsu Key Laboratory of Artificial Functional Materials, College of Engineering and Applied Sciences and Collaborative Innovation Center of Advanced Microstructures, Nanjing University, Nanjing, China*
2. *School of Optical and Electronic Information, Huazhong University of Science and Technology, Wuhan, China.*
3. *Wuhan National Laboratory for Optoelectronics, Huazhong University of Science and Technology, Wuhan, China.*
4. *Physical Measurement Laboratory, National Institute of Standards and Technology, Gaithersburg, MD, USA*
5. *Maryland NanoCenter, University of Maryland, College Park, MD, USA*

Supplementary Note 1: Phase contrast imaging using spiral phase masking function

In this work, $(u,\ v)$ and $(x,\ y)$ are the spatial coordinates at the metasurface (Fourier) and object (image) planes, respectively. (ρ, ϕ) and $(r,\ \varphi)$ are their polar coordinates that have the relation of $\begin{cases} \rho = \sqrt{u^2 + v^2} \\ \phi = \arctan(v/u) \end{cases}$ and $\begin{cases} r = \sqrt{x^2 + y^2} \\ \varphi = \arctan(y/x) \end{cases}$. Based on the imaging process of a 4f system, the output light field $E_{out}(x, y)$ of the object place and input light field $E_{in}(x, y)$ of the image plane can be associated by the spatial filter $M(\rho, \phi)$, and have the following relation,

$$E_{out}(x, y) = E_{in}(x, y) \otimes F\{M(\rho, \phi)\} = E_{in}(x, y) \otimes m(r, \varphi) \tag{S1}$$

Here, the symbol $\otimes$ represents convolution and $F\{\cdot\}$ denotes the Fourier transform of the masking function, $m(r, \varphi)$ is the point-spread function (PSF) that determines the filtering effect of the system and can be written as [1],

$$m(r, \varphi) = \frac{1}{i\lambda f} \int_0^{2\pi} \int_0^{\infty} M(\rho, \phi) \exp\left[-\frac{ik}{f} r\rho \cos(\phi - \varphi)\right] \rho d\rho d\phi \tag{S2}$$

where $k = 2\pi/\lambda$ is the light wave vector, f is the focal length of the lens. Considering a spiral phase mask filter of a circular aperture with radius *R*,

$$M_2(\rho, \phi) = exp(i\phi) \tag{S3}$$

According to Eq. (S2), the PSF of the filter can finally be expressed as,

$$m_2(r, \varphi) = -\frac{k}{f} \exp(i\varphi) \int_0^R J_1\left(\frac{kr\rho}{f}\right) \rho d\rho \tag{S4}$$

Combined with the recurrence relation of the Bessel function [2, 3], it can be deduced as follows,

$$m_2(r, \varphi) = -\frac{\pi R}{2r} [J_1(\tau) H_0(\tau) - J_0(\tau) H_1(\tau)] \exp(i\varphi) \tag{S5}$$

where $\tau = kRr/f$. J_0 and J_1 are Bessel functions of zero and first order, respectively. H_0 and H_1 are Struve functions of zero and first order, respectively. The PSF (m_2) can be regarded as the formation of a vortex that has a doughnut shaped intensity distribution and a spiral phase profile changing from 0 to 2π for one turn. Then the output field obtained at the object plane of 4f system is written as,

$$E_{out}(x, y) = E_{in}(x, y) \otimes m_2(r, \varphi) = -E_{in}(x, y) \otimes \frac{\pi R}{2r} [J_1(\tau) H_0(\tau) - J_0(\tau) H_1(\tau)] \exp(i\varphi) \tag{S6}$$

In the convolution process of Eq. (S6), the $m_2(r, \varphi)$ with vortex element will be weighted to superimpose on each point of input light field $E_{in}(x, y)$, and then integrated over the whole area to determine the amplitude of the corresponding point of output light field $E_{out}(x, y)$. Due to the phase difference of π in the opposite azimuth of the vortex element, integrating the uniform area of E_{in} will lead to destructive interference and a dark background. In contrast, arbitrarily unevenness in the region of integration including

amplitude gradient and phase gradient will remove the destructive interference and result in bright regions. On the other hand, assuming incident field $E_{in}(x,y) = |E_{in}|\exp(i\psi_{in})$, the spiral phase filtering properties also can be quantified by Taylor expanding E_{in} and solving Eq. (S6) [4],

$$E_{out} \propto \exp(i\psi_{in})G_A \exp(i\delta_A) + iE_{in}G_P exp(i\delta_P) \tag{S7}$$

where G_A and G_P (δ_A and δ_P) are the magnitudes (phase) of the gradients of the input field amplitude and the input filed phase, respectively:

$$\boldsymbol{G_A} = \nabla|E_{in}| = G_A exp(i\delta_A)\boldsymbol{e_A} \tag{S8}$$

$$\boldsymbol{G_P} = \nabla|\psi_{in}| = G_P exp(i\delta_P)\boldsymbol{e_P} \tag{S9}$$

The output field of Eq. (S7) consists of two terms that describe the effects of amplitude and phase variations of the input field in spiral phase filtering. The two terms are proportional to the absolute values of the gradients $\boldsymbol{G_A}$ and $\boldsymbol{G_P}$ respectively, which results in strong isotropic enhancement of amplitude and phase edge. In additional, combining with the analytical result of eq. (S7), it shows that the spiral phase filtering operation is equivalent to the two-dimensional spatial differentiation of incident light field in principle. The corresponding spatial spectral transfer function can be calculated by the relation of $H(k_x, k_y) = E_{out}(u,v)/E_{in}(u,v)$ and shown in Fig. S1.

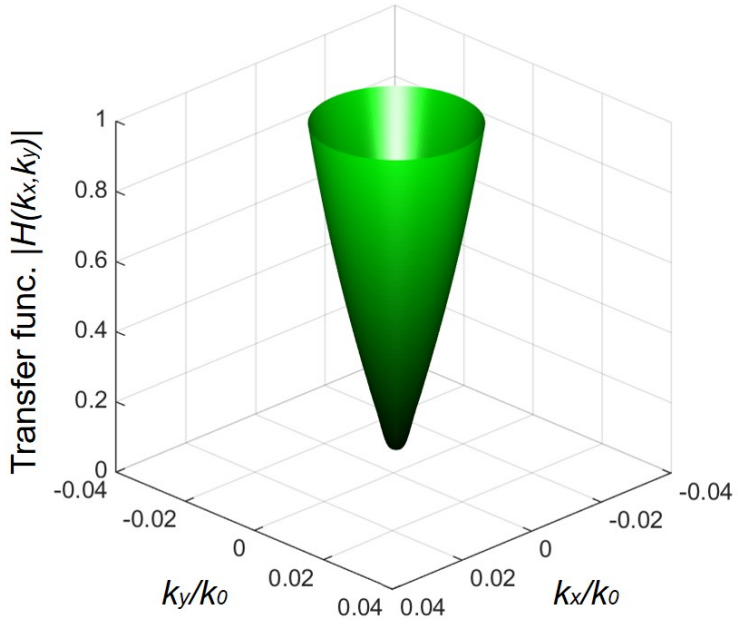

Figure S1. The calculated spatial spectral transfer function of the spiral phase filtering operation.

Supplementary Note 2: Derivation of the Jones matrix J and its eigenvalues and eigenvectors.

Assuming light incident upon the planar optical metasurface filter is in two orthogonal spin states $|L\rangle = \frac{1}{\sqrt{2}}\begin{bmatrix}1\\ i\end{bmatrix}$ and $|R\rangle = \frac{1}{\sqrt{2}}\begin{bmatrix}1\\ -i\end{bmatrix}$, where $|L\rangle$ and $|R\rangle$ denote left- and right-circular polarization (LCP and RCP) in the linear polarization basis. In order to independently implement two different masking function ($M_1(\rho,\phi) = exp(ic_0)$ and $M_2(\rho,\phi) = exp(i\phi)$, with c_0 being a constant) for the incident plane wave propagating along the *z*-direction respectively in LCP and RCP states, the optical metasurface should be described by a Jones matrix *J* that simultaneously satisfies,

$$J(\rho,\phi)|L\rangle = M_1(\rho,\phi)|R\rangle \tag{S10}$$

and

$$J(\rho,\phi)|R\rangle = M_2(\rho,\phi)|L\rangle \tag{S11}$$

Upon matrix inversion of Eq. (S10) and (S11) we obtain the form as

$$J(\rho,\phi) = \begin{bmatrix} M_1 & M_2 \\ -iM_1 & iM_2 \end{bmatrix}\begin{bmatrix} 1 & 1 \\ i & -i \end{bmatrix}^{-1} \tag{S12}$$

Then, we can show that the desired matrix J is

$$J(\rho,\phi) = \frac{1}{2}\begin{bmatrix} (M_1+M_2) & -i(M_1-M_2) \\ -i(M_1-M_2) & -(M_1+M_2) \end{bmatrix} \tag{S13}$$

The unitary of this matrix guarantees that it can be decomposed into the following form $J = \gamma\Delta\gamma^{-1}$, where γ is a real unitary matrix whose columns are the eigenvectors of J, and Δ is a diagonal matrix whose elements are the eigenvalues of J. By solving the characteristic equation of the Jones matrix J, we can find its eigenvalues as,

$$\xi_1 = e^{i[\frac{1}{2}(c_0+\phi)]} \qquad \xi_2 = e^{i[\frac{1}{2}(c_0+\phi)-\pi]} \tag{S14}$$

and eigenvectors as

$$|\lambda_1\rangle = \begin{bmatrix} \cos\frac{1}{4}(c_0-\phi) \\ sin\frac{1}{4}(c_0-\phi) \end{bmatrix} \quad |\lambda_2\rangle = \begin{bmatrix} -\sin\frac{1}{4}(c_0-\phi) \\ cos\frac{1}{4}(c_0-\phi) \end{bmatrix} \tag{S15}$$

Thus, the Jones matrix can be decomposed into the following form,

$$J(\rho,\phi) = \gamma\Delta\gamma^{-1} =$$
$$\begin{bmatrix} \cos\frac{1}{4}(c_0-\phi) & -\sin\frac{1}{4}(c_0-\phi) \\ sin\frac{1}{4}(c_0-\phi) & cos\frac{1}{4}(c_0-\phi) \end{bmatrix}\begin{bmatrix} e^{i[\frac{1}{2}(c_0+\phi)]} & 0 \\ 0 & e^{i[\frac{1}{2}(c_0+\phi)-\pi]} \end{bmatrix}\begin{bmatrix} \cos\frac{1}{4}(c_0-\phi) & \sin\frac{1}{4}(c_0-\phi) \\ -sin\frac{1}{4}(c_0-\phi) & cos\frac{1}{4}(c_0-\phi) \end{bmatrix} \tag{S16}$$

Since Jones matrix J works in the linear polarization basis and γ can be regarded as a rotation matrix for

the matrix Δ, In contrast to a normal linear birefringent wave-plate rotated through some angle θ, the values of phase shifts φ_x and φ_y along the two symmetry axes and θ all depend on the spatial coordinate, and can be written as the analytical expression,

$$\varphi_x = \frac{1}{2}(c_0 + \phi) \tag{S17}$$

$$\varphi_y = \frac{1}{2}(c_0 + \phi) - \pi \tag{S18}$$

$$\theta = \frac{1}{4}(c_0 - \phi) \tag{S19}$$

The phase difference π between φ_x and φ_y requires the element structure of the metasurface to act as a half wave plate (HWP). Based on the Eq. (S17) - (S19), the dependence of phase shifts (φ_x, φ_y) and the rotation angle θ of the HWPs on the spatial coordinates in the metasurface device are calculated and shown in Fig. S1.

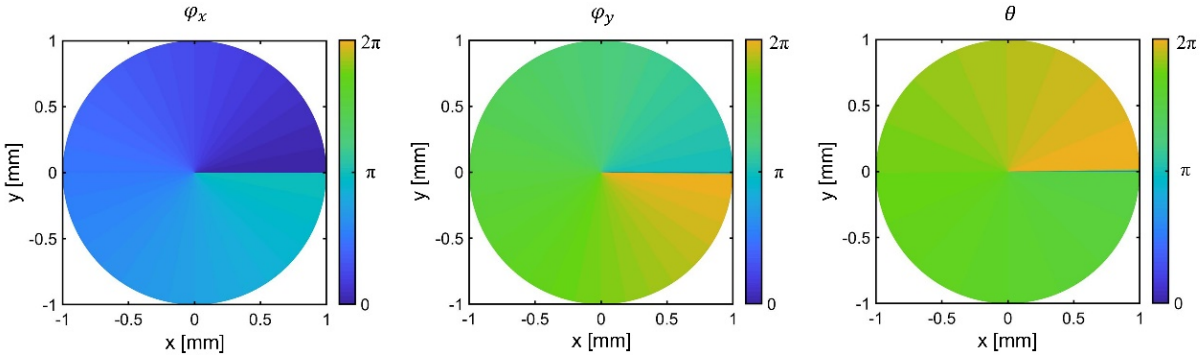

Figure S2. Calculated phase shifts φ_x and φ_y along the two symmetry axes of HWPs and the rotational angle θ as a function of the spatial coordinate with $C_0 = 0$.

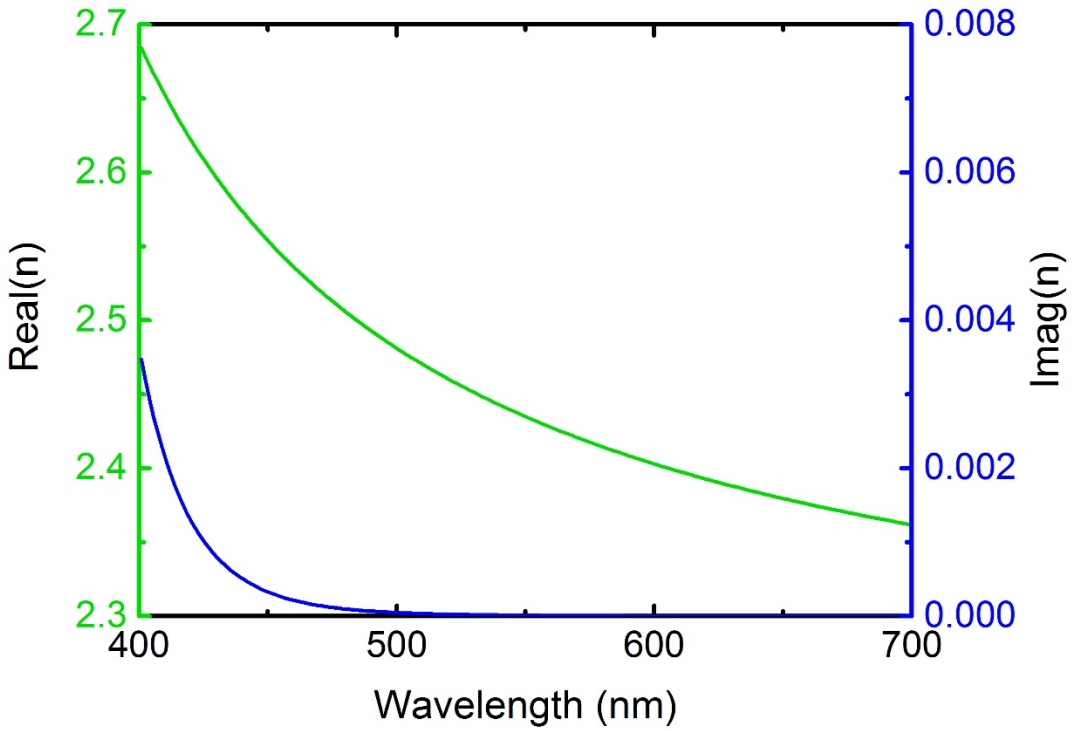

Figure S3. Refractive index of atomic layer deposition (ALD) TiO_2. The real and imaginary part of the refractive index (*n*) of 64 nm thick ALD TiO_2 is measured using spectroscopic ellipsometry.

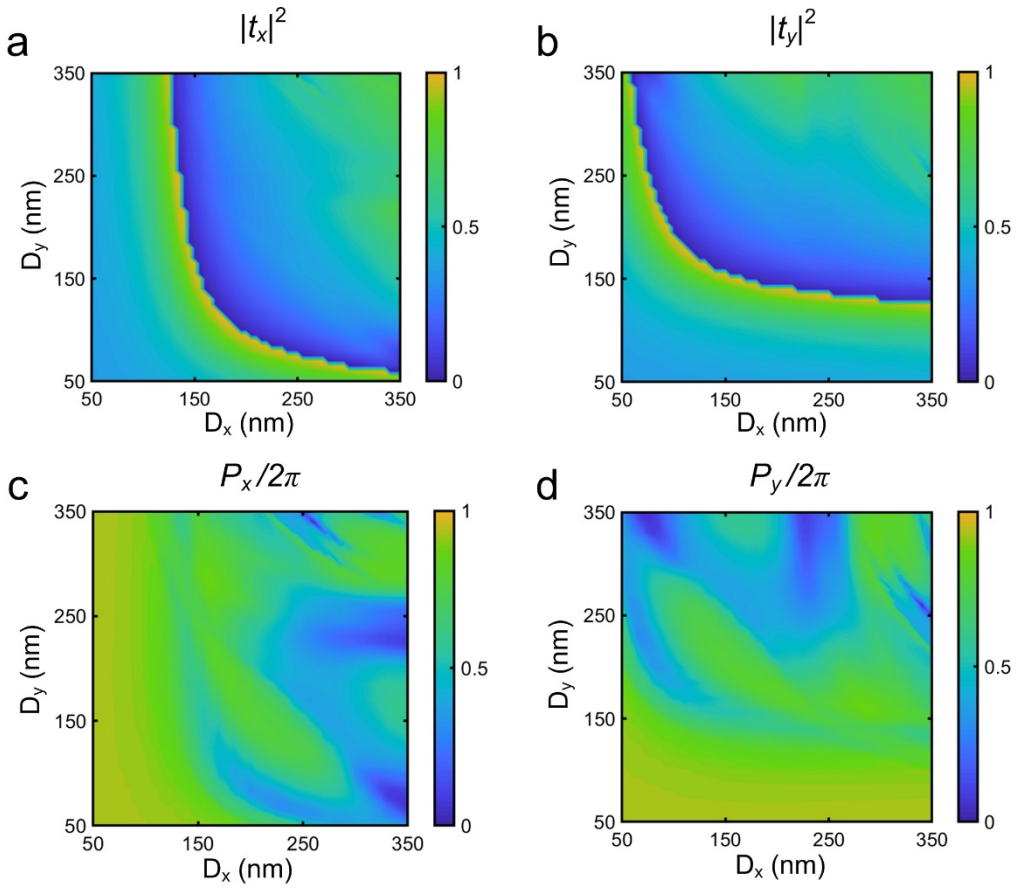

Figure S4. Simulated normalized intensity transmission coefficients and phase shifts as a function of rectangular nanopillar dimensions at the wavelength of 530 nm. Intensity transmission coefficients ($|t_x|^2$and$|t_y|^2$) and the phase (P_x and P_y) of x and y-polarized optical waves for the periodic array of TiO_2 rectangular nanopillars with $\theta = 0$. Each point in the spectra map corresponds to a nanopillar with a specific (D_x, D_y) combination.

Supplementary Note 3: Effect of the segment number of spiral phase on imaging

The perfect masking function $M_2(\rho,\phi)$ presented in eq. (S3) has a continuous and smooth phase. In fact, the one imparted on the metasurface filter is discretized and can be written as,

$$M_2(\rho,\phi) = exp(i\mathrm{fix}(\frac{n\phi}{2\pi})\frac{2\pi}{s}) \tag{S20}$$

where $(\rho,\ \phi)$ is the polar coordinate, *s* denotes the segment number of masking function M_2 imparted on the metasurface filter. fix(X) can round the elements of X to the nearest integers towards zero. In Fig. S5, we calculate the phase contrast imaging using the spiral phase function with segment number of 1, 4, 8, 16, respectively. They show that the imaging results gradually approach the perfect spiral phase contrast imaging with the increase of the segment number. On the other hand, in order to quantify the effect of segment number (*s*) in spiral phase on imaging quality and obtain the proper degree of discretization of HWPs in the full range [0, 2π], the mean square error (*MSE*) function has been adopted as,

$$MSE(s) = \frac{\sum_{a=1}^{A}\sum_{b=1}^{B}|I(a,b)-I_s(a,b)|^2}{A\times B} \tag{S21}$$

where $I(a,b)$ and $I_s(a,b)$ represent the imaging results by adopting a perfect and the *s*-segment spiral phase filter, respectively. A and B are the sampling number of the image in plane dimension. The *MSE* curve between the imaging results obtained using a perfect spiral phase and the spiral phase with different step numbers is calculated and shown in Fig. S6. The *MSE* has been reduced to a negligible value with the segment number $s \geqslant 16$. After a comprehensive analysis of imaging quality and design difficulty, s = 16 is selected as the segment number of masking function.

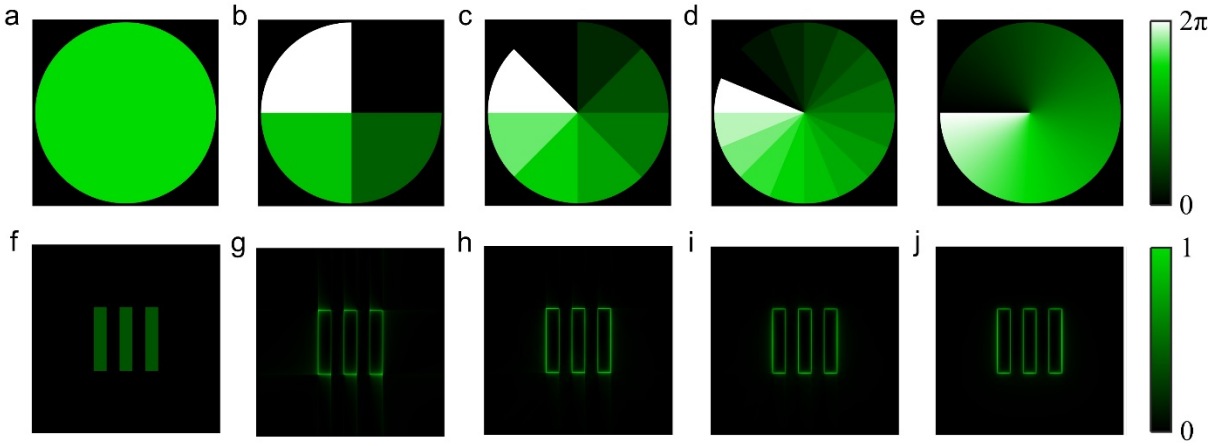

Figure S5. Calculated phase contrast imaging using the spiral phase filter with different segment number. a-d, show the phase distribution of the spiral phase filter with the segment number of 1, 4, 8, 16, respectively. **e**, The phase distribution of a perfect spiral filter. **f-j**, The corresponding imaging results. The imaging results gradually approach the perfect spiral phase contrast imaging with the increase of the segment number.

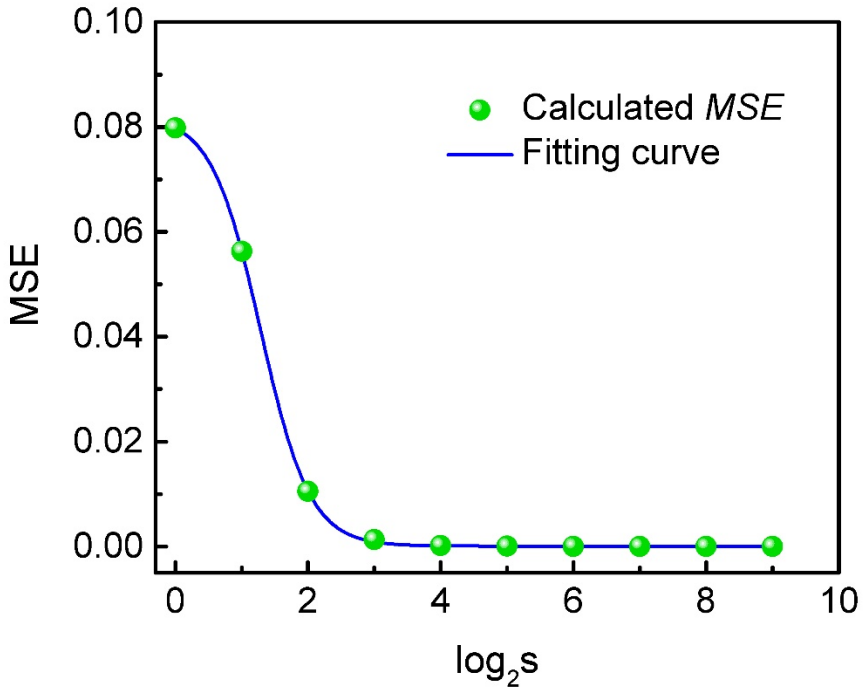

Figure S6. Calculated mean square error function (MSE) curve between the imaging results obtained using a perfect spiral phase and the spiral phase with different step numbers. The curve can be used to quantify the effect of steps number (*s*) in spiral phase on imaging quality and determine the degree of discretization of HWPs in the full range [0, 2π].

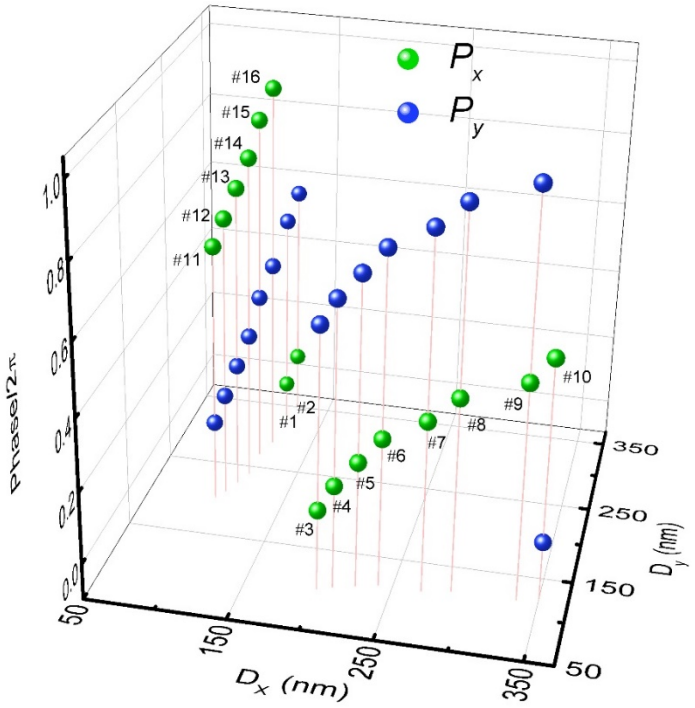

Figure S7. The dimension distribution and phase shifts of the chosen TiO_2 rectangular nanopillars at the wavelength of 530 nm. Green and blue spheres mark the phase shifts (P_x and P_y,) of the chosen 16-level nanopillars. Each level corresponds to a specific TiO_2 nanopillar HWP. The structural parameters of the nanopillars are optimized so that the transmission coefficients and polarization conversion efficiencies are high enough across the full visible region.

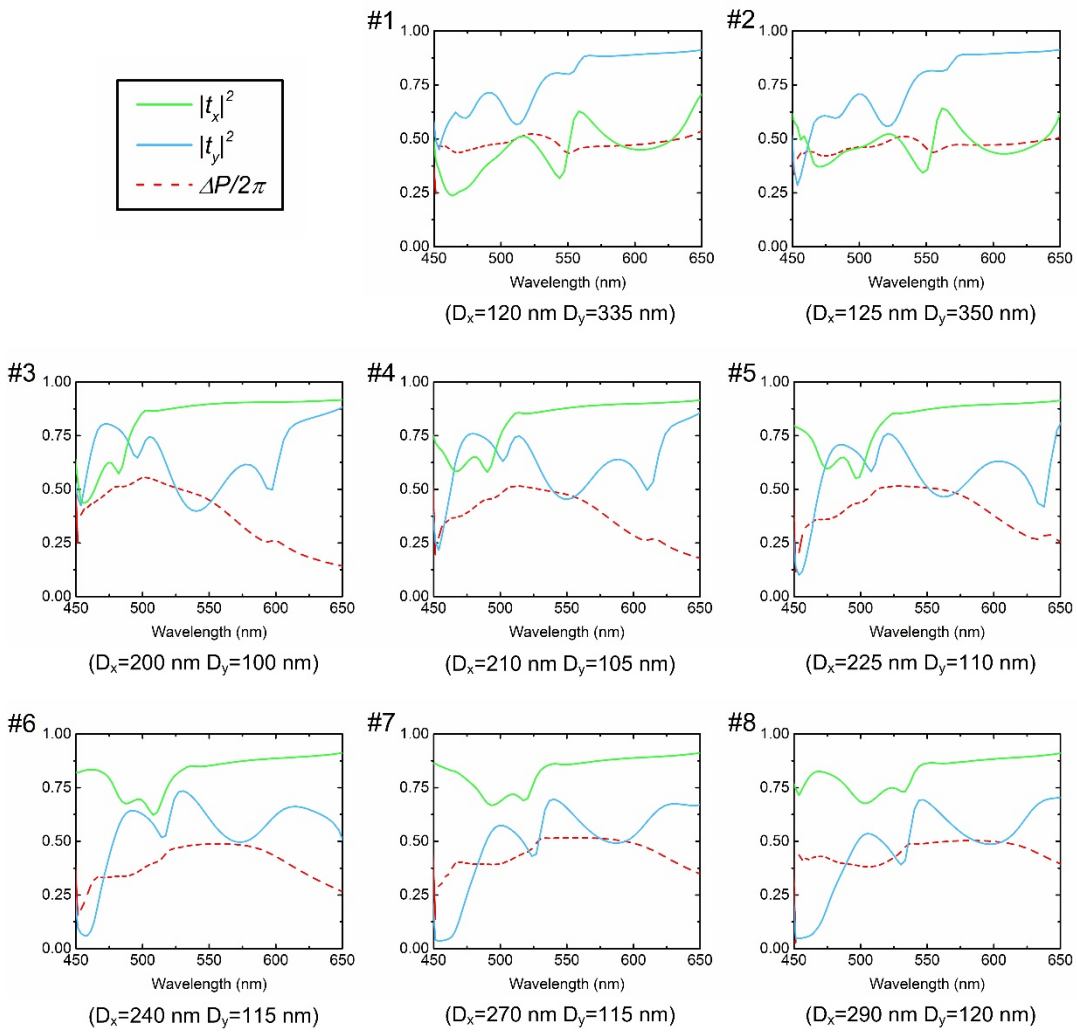

Figure S8. Wavelength dependence of the intensity transmission coefficients ($|t_x|^2$ and $|t_y|^2$) and the phase difference ($\Delta P = P_x - P_y$) of *x* and *y*-polarized optical waves for periodic arrays of selected nanopillars. The spectra are shown for eight nanopillars with different (D_x, D_y) combination: #1 (120 nm, 335 nm), #2 (125 nm, 350 nm), #3 (200 nm, 100 nm), #4 (210 nm, 105 nm), #5 (225 nm, 110 nm), #6 (240 nm, 115 nm), #7 (270 nm, 115 nm), #8 (290 nm, 120 nm). The transmission and phase spectra for the remaining eight nanopillars can be obtained by swapping *x* and *y* in the spectra graphs.

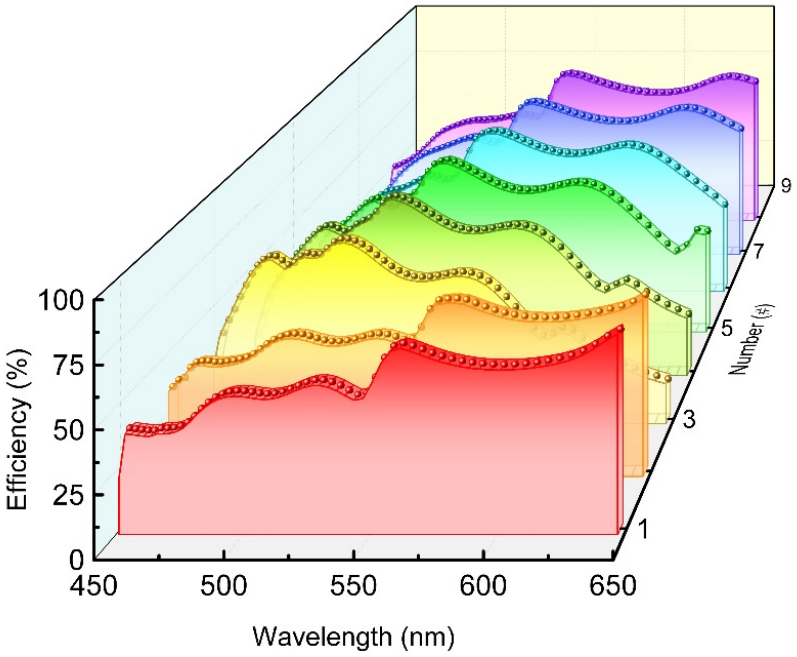

Figure S9. Calculated polarization conversion efficiency for the selected eight rectangular nanopillars in the entire visible range. The structural parameters of the nanopillars are optimized so that the transmission coefficients and polarization conversion efficiencies for the incident light are high enough across the full visible region. The remaining eight rectangular nanopillars have the same polarization conversion efficiency as the ones given in the spectra.

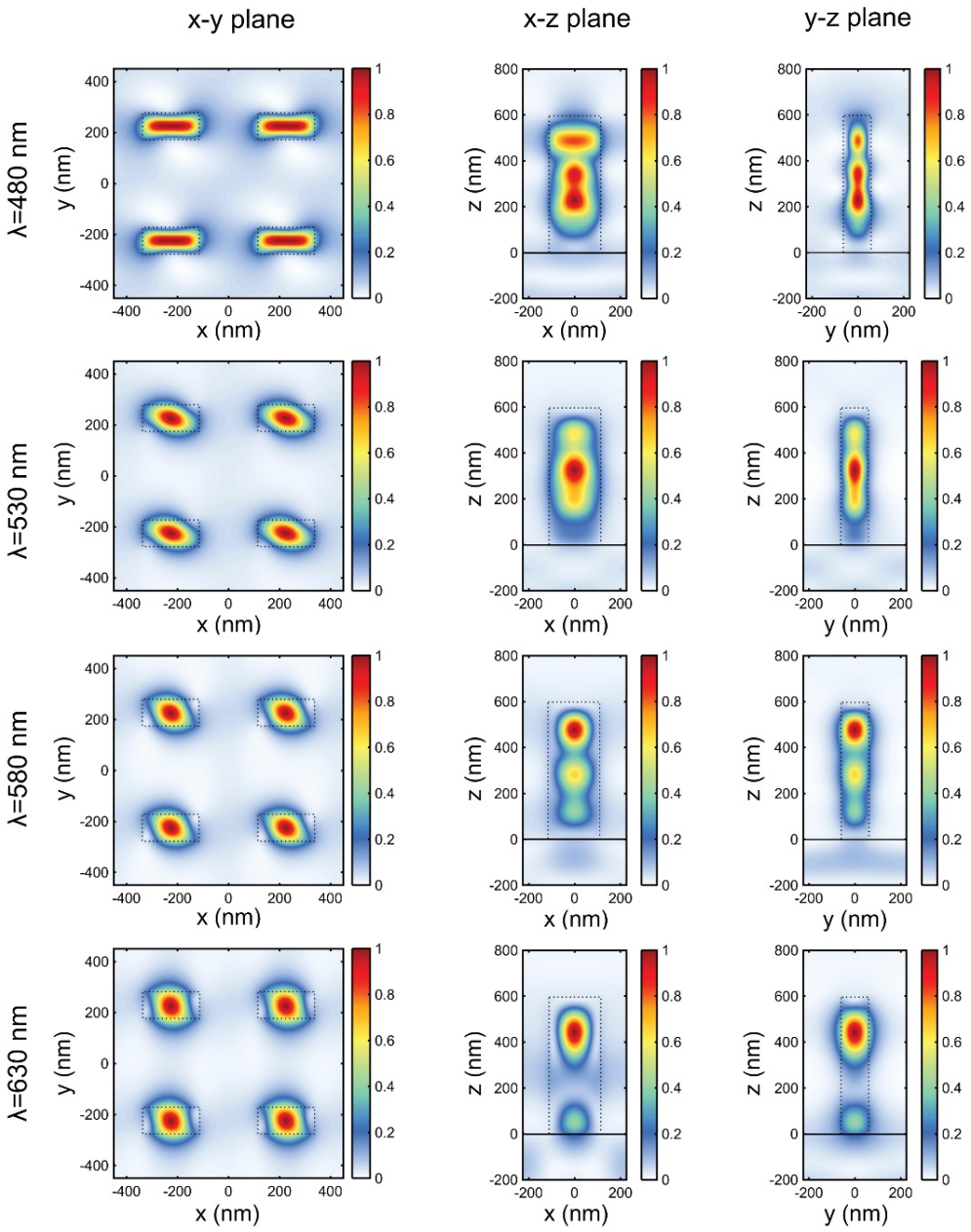

Figure S10. The normalized magnetic energy density distribution of the nanopillars periodic arrays for LCP plane wave illumination at the wavelength of 480 nm, 530 nm, 580 nm, and 630 nm, respectively. Top views (left: *x*-*y* plane) and side views (middle: *x*-*z* plane and right: *y*-*z* plane). The results show that the normalized magnetic energy density is mainly confined inside the TiO_2 nanopillar. The coupling effect between neighboring nanopillars is very weak.

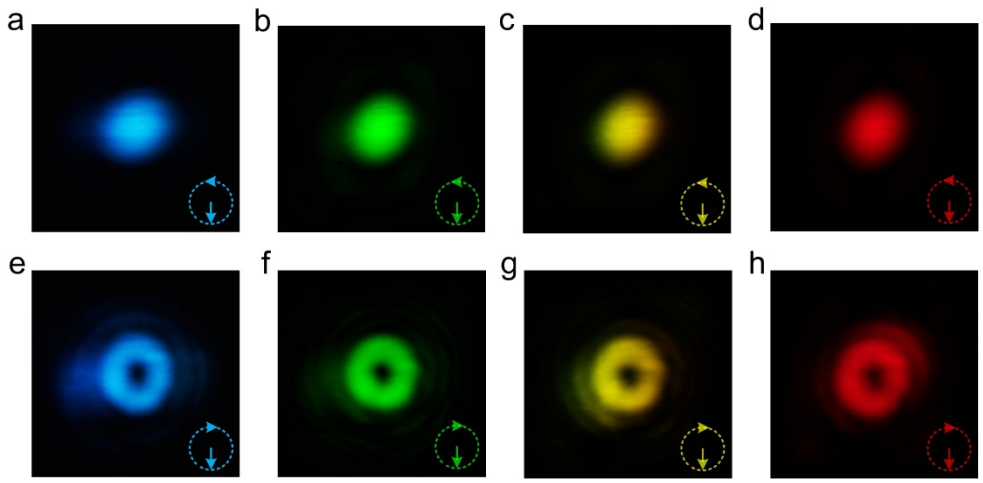

Figure S11. Measured intensity distributions of output states for LCP and RCP incident light illumination at the wavelength of 480 nm, 530 nm, 580 nm, and 630 nm. a-d, show a Gaussian distribution for LCP incident light and **e-h**, show the donut intensity distribution for RCP incident light, which demonstrate that the spin-dependent metasurface spatial filter is able to implement two independent masking functions in the entire visible frequency.

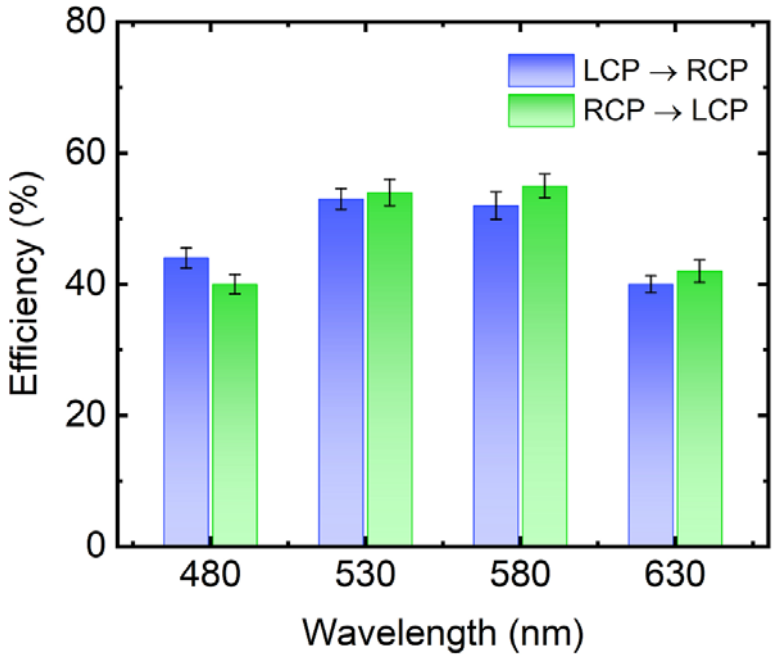

Figure S12. The measured conversion efficiency of the metasurface device for LCP and RCP incident light illumination at the wavelength of 480 nm, 530 nm, 580 nm, and 630 nm, respectively. Error bars: standard deviation for four repeated experimental measurements. The high conversion efficiency is mainly due to low-loss material selection of TiO_2 and parameters optimization of HWPs-nanopillars. The measurement error bars mainly come from the impurity of chiral incident and output beams.

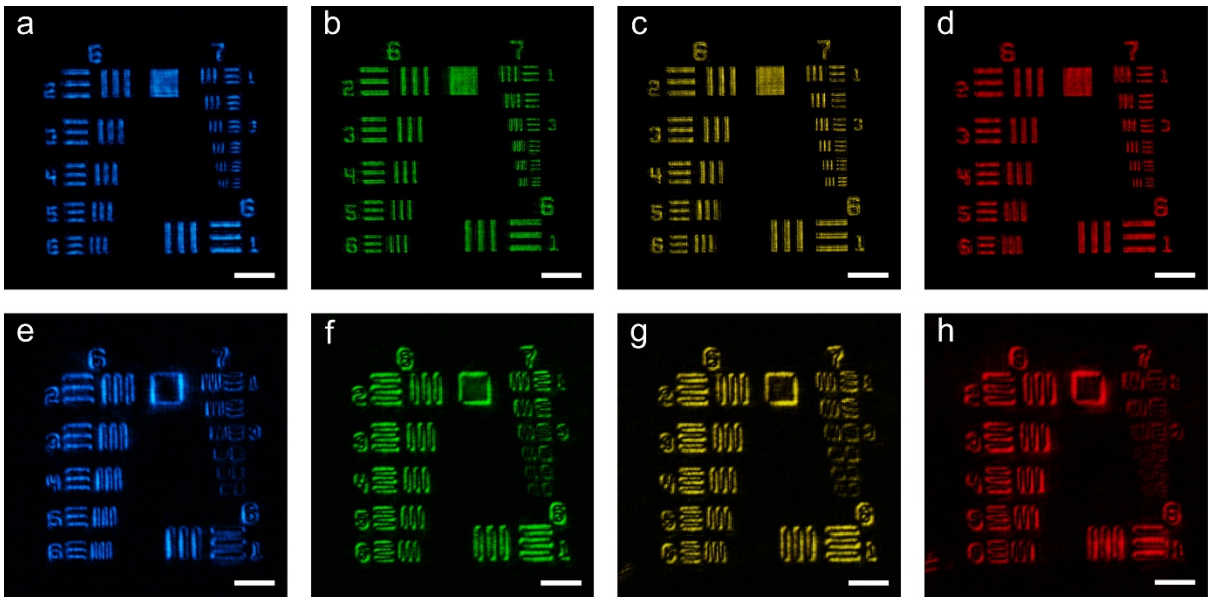

Figure S13. Investigation of the system resolution for two imaging modes in the visible region. a-d, the bright-field imaging mode at the wavelength of 480 nm, 530 nm, 580 nm, and 630 nm, respectively, the smallest line pair that can be resolved in the resolution test chart is elements 6 of group 7 (228 lp/mm), which corresponds a resolution of 2.19 μm along the *x* and *y* direction. **e-f**, for phase contrast imaging mode, the smallest line pair that can be resolved in the resolution test chart is elements 3 of group 7 (161 lp/mm), which corresponds to a resolution of 3.11 μm. Scale bar: 50 μm.

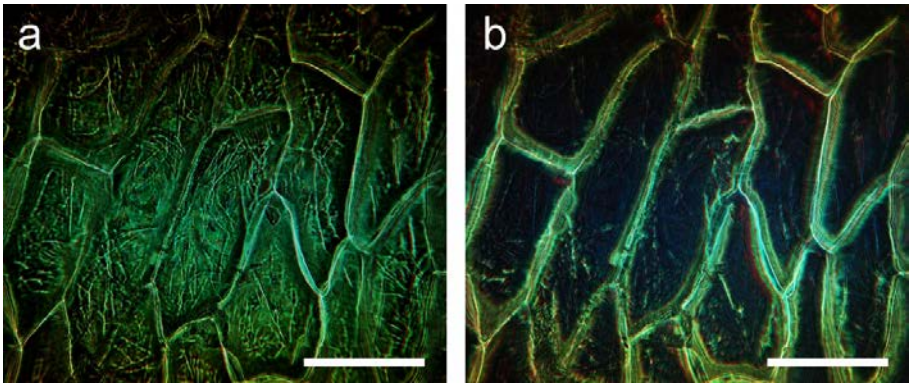

Figure S14. The bright-field and edge-enhanced phase contrast images of the undyed onion epidermal cells illuminated by a white light beam. Images are captured with a 20 × objective lens. a, Traditional bright-field images for LCP plane wave illumination. **b**, Edge-enhanced phase contrast images for RCP plane wave illumination. Scale bar: 100 μm.

Supplementary Reference

[1] G. O. Reynolds, J. B. Develis, and B. J. Thompson, *The New Physical Optics Notebook: Tutorials in Fourier Optics* (SPIE, 1989).

[2] M. Abramowitz and I. A. Stegun, *Handbook of Mathematical Functions with Formulas, Graphs, and Mathematical Tables* (Dover, 1970).

[3] S. N. Khonina, V. V. Kotlyar, M. V. Shinkaryev, V. A. Soifer, and G. V. Uspleniev, The phase rotor filter, *J. Mod. Opt.* **39**, 1147–1154 (1992).

[4] A. Jesacher, S. Furhapter, S. Bernet, and M. Ritsch-Marte, Spiral interferogram analysis, *J. Opt. Soc. Am. A* **23**, 1400-1409 (2006).